PNAS RESEARCH ARTICLE | EARTH, ATMOSPHERIC, AND PLANETARY SCIENCES

Ionizing radiation exposure on Arrokoth shapes a sugar world

Chaojiang Zhang[a,b], Vanessa Leyva[c], Jia Wang[a,b], Andrew M. Turner[a,b], Mason Mcanally[a,b], Ashanie Herath[a,b], Cornelia Meinert[c,1], Leslie A. Young[d,1], and Ralf I. Kaiser[a,b,1]

Edited by Imke de pater, University of California, Berkeley, CA; received November 17, 2023; accepted April 18, 2024 by Editorial Board Member Michael Manga

The Kuiper Belt object (KBO) Arrokoth, the farthest object in the Solar System ever visited by a spacecraft, possesses a distinctive reddish surface and is characterized by pronounced spectroscopic features associated with methanol. However, the fundamental processes by which methanol ices are converted into reddish, complex organic molecules on Arrokoth's surface have remained elusive. Here, we combine laboratory simulation experiments with a spectroscopic characterization of methanol ices exposed to proxies of galactic cosmic rays (GCRs). Our findings reveal that the surface exposure of methanol ices at 40 K can replicate the color slopes of Arrokoth. Sugars and their derivatives (acids, alcohols) with up to six carbon atoms, including glucose and ribose—fundamental building block of RNA—were ubiquitously identified. In addition, polycyclic aromatic hydrocarbons (PAHs) with up to six ring units ($^{13}C_{22}H_{12}$) were also observed. These sugars and their derivatives along with PAHs connected by unsaturated linkers represent key molecules rationalizing the reddish appearance of Arrokoth. The formation of abundant sugar-related molecules dubs Arrokoth as a sugar world and provides a plausible abiotic preparation route for a key class of biorelevant molecules on the surface of KBOs prior to their delivery to prebiotic Earth.

Arrokoth | sugars | colors | ultrared matter

Significance

The flyby of the New Horizons spacecraft of the Kuiper Belt Object Arrokoth revealed its reddish appearance and unraveled the unexpected presence of a methanol-rich surface. However, the chemical compositions and fundamental processes responsible for the surface coloring have remained ambiguous. Here, we have evidence that methanol ices exposed to galactic cosmic rays can replicate the colors of Arrokoth. Organics formed indicate that Arrokoth is rich in sugars including biologically significant ribose and glucose, while aromatic hydrocarbons are essential in producing the ultrared color slopes. Our findings provide insights into the surface evolution of planetesimals in the early Solar System ranging from the Kuiper Belt to Oort's clouds as repositories of short and long-periodic comets.

The New Horizons mission to the Kuiper Belt (1–3)—a vast region beyond the orbit of Neptune at 30 AU (astronomical unit) to about 50 AU from the Sun—has revolutionized our understanding of the origin and evolution of the Solar System (4–10). The Kuiper Belt encompasses more than 100,000 ice-rich objects (KBOs) with surfaces covered by frozen volatiles like nitrogen (N_2) (Pluto), methane (CH_4) (Makemake), water (H_2O) plus ammonia (NH_3) (Orcus and Quaoar), and methanol (CH_3OH) (Arrokoth and 2002 VE_{95}) (11). The New Horizons spacecraft has explored the contact binary Arrokoth (2014 MU_{69})—the farthest object in the Solar System ever visited by a spacecraft—uncovering extraordinary geological features such as troughs and hills, as well as a reddish appearance with color slopes ranging from 20 to 32% per 100 nm (7–9). Color slopes define a quantitative measure of the dependence of the reflectance on the wavelength (12). A detailed analysis of New Horizons Ralph Linear Etalon Infrared Spectral Array (LEISA) images identified signatures associated with methanol ice from 2.27 to 2.34 μm (4,405 to 4,273 cm^{-1}) (9). This finding underpinned the detection of a functionalized hydrocarbon (alcohol) on the surface of a KBO (13). However, the underlying processes, which convert methanol ices to Arrokoth's ultrared surface, along with the nature of the chromophores, i.e., the functional groups of a molecule that absorb visible light responsible for its coloring, have represented a fundamental puzzle for planetary scientists (14–17).

This detailed understanding of the origin of Arrokoth's reddish appearance together with the spectroscopic and chemical evolution of the cold surfaces at about 42 K is vital to the planetary science and astrobiology communities (18, 19). The low-temperature synthesis of complex carbon-, hydrogen-, and oxygen-bearing molecules in the surface layers can modify the reflection spectra of Arrokoth (9). Gaining a fundamental knowledge of the synthesis processes involved in these organic compounds can not only shed light on the complex chemistry of Arrokoth's surface, but also provide facilitated access to the comprehensive inventory of astrobiological molecules within the Kuiper Belt. This expansion involves extrapolating from our idealized system to a more complex mixture, thereby broadening our insights. Some of these molecules, such as carbohydrates, hold key functions in biochemistry, serving as energy sources, contributing to metabolism, and acting as molecular building blocks in DNA and RNA (20–22). Dynamical simulations of the Solar System reveal that KBOs such as Arrokoth are a source of short-period comets, which could have delivered biologically important molecules such as carbohydrates to the early Earth (23, 24). Hence, an understanding of the chemical evolution of KBO such as

Author contributions: C.M., L.A.Y., and R.I.K. designed research; C.Z., J.W., A.M.T., M.M., and A.H. performed research; V.L., C.M., L.A.Y., and R.I.K. contributed new reagents/analytic tools; C.Z. and V.L. analyzed data; and C.Z., C.M., L.A.Y., and R.I.K. wrote the paper.

The authors declare no competing interest.

This article is a PNAS Direct Submission. I.d.p. is a guest editor invited by the Editorial Board.

[1]To whom correspondence may be addressed. Email: Cornelia.MEINERT@univ-cotedazur.fr, layoung@boulder.swri.edu, or ralfk@hawaii.edu.

This article contains supporting information online at https://www.pnas.org/lookup/suppl/doi:10.1073/pnas.2320215121/-/DCSupplemental.

Published June 3, 2024.

Arrokoth's methanol-rich surface provides fundamental clues on the origin of astrobiological molecules in our Solar System.

Planetary scientists proposed that Arrokoth's reddish appearance is attributed to the presence of *tholins* (9, 25), a term coined by Carl Sagan defining refractory, polymer-like complex organics (26). Two sources of these *tholins* have been hypothesized (27). One is the primordial (organic) submicron particles formed in the presolar disk and condensed prior to being scattered to the current position of the Kuiper Belt as leftover debris from the early formation of the Solar System (28). Alternatively, *tholins* represent chemical products of the interaction of primitive surface ices such as Arrokoth's methanol with ionizing radiation from the solar wind and galactic cosmic rays (GCRs) (29, 30). These products may undergo resurfacing processes and could also in principle modify the surface color of KBOs (31–36). Laboratory simulation experiments have shown that methanol ices present a trend of increasing spectral slopes during the irradiation by charged particles as proxies of the solar wind and GCRs (37, 38). On the molecular level, as a potential precursor to complex organics on interstellar dust in cold molecular clouds, the energetic processing of methanol-containing ice mixtures has been implicated in the synthesis of sugar-related molecules like glycolaldehyde ($CHOCH_2OH$) (*SI Appendix*, Table S1) (39–42). However, a systematic strategy capable of unraveling the physical and chemical changes occurring on Arrokoth's surface ices (methanol) upon exposure to ionizing radiation is still lacking. This includes understanding its surface colors and establishing a comprehensive inventory of molecular carriers and chromophores formed from the early stages to the present through irradiation processes.

Here, we merge laboratory irradiation experiments with a complementary suite of spectroscopic diagnostics to investigate the physical and chemical processing that triggers the reddening of methanol-rich surfaces of KBOs such as Arrokoth. This work endeavors to categorize molecular carriers alongside their chromophores and leverage these findings to provide fundamental insights into the origins of color evolution at the molecular level on methanol-rich KBOs. Since the laboratory exposure time of KBO analog ices can be scaled to the time of the radiation processing of a KBO surface (43), this affords a thorough investigation of how the original state and chemical reactions influence the colors and compositions of KBOs (44–47). The estimated time for the radiation dose accumulation to reach 1 eV amu^{-1} at the KBO surface of about 100 nm is ~2.4×10^7 y (48). It is worth noting that accumulating 1 eV amu^{-1} at about 100 μm requires about 8×10^8 y (49), which is roughly 30 times longer than the time needed to alter the top layers of ice by hundreds of nanometers. By initially concentrating on a population of KBOs with methanol-rich surfaces such as Arrokoth as a testbed, this strategy will ultimately unravel the effect of the chemical composition on the color diversity of KBOs. Therefore, in our experiments, methanol and its primary radiolysis product carbon monoxide (50) were exposed to GCR proxies, i.e., 5 keV electrons. These energetic electrons simulate secondary electrons formed as GCRs traverse the Kuiper Belt (*Methods*), at KBO-relevant temperatures below 40 K. The radiation doses applied (*SI Appendix*, Table S2) mimic an exposure of Arrokoth's surface equivalent to approximately 1,800 My. Note that, we used ^{13}C–labeled methanol ($^{13}CH_3OH$) and carbon monoxide ($^{13}C^{18}O$) in these irradiation experiments to rule out any possible contamination during the manipulation of residues and the analytical procedure. During the irradiation, the color slopes and functional groups were recorded in situ utilizing ultraviolet-visible (UV-vis) spectroscopy and Fourier transform infrared (FTIR) spectroscopy, respectively. The organic residues, which develop during the temperature-programmed desorption (TPD), were analyzed by two-dimensional gas chromatography coupled with time-of-flight mass spectrometry (GC×GC–TOF-MS) and time-of-flight secondary ion mass spectrometry (TOF-SIMS) to probe newly synthesized species in the processed Arrokoth model ices such as monosaccharides and their derivatives. These investigations clearly show that laboratory-processed methanol ices at 40 K replicate the color slopes of Arrokoth exposed to GCRs for at least 1,300 My. Monosaccharides and sugar-related compounds containing up to six carbon atoms such as glucose ($^{13}C_6H_{12}O_6$), allose ($^{13}C_6H_{12}O_6$), mannitol ($^{13}C_6H_{12}O_6$), and ribose ($^{13}C_5H_{10}O_5$), some of which are incorporated as molecular building blocks in RNA and lipids, were identified in the residues of exposed methanol ices. Various polycyclic aromatic hydrocarbons (PAHs) along their fragments carrying up to six ring units were also observed in the residues. These sugars and their derivatives along with PAHs connected by unsaturated linkers are key components in producing the reddish appearance of Arrokoth. The formation of sugar (related) organics affords persuasive evidence of the GCR-triggered abiotic transformation of converting methanol ices into monosaccharides and possibly polysaccharides classifying Arrokoth as a sugar world and provides a plausible source of this key class of prebiotic molecules for the evolution of life on early Earth.

Results

UV-Vis Spectroscopy. UV-vis spectroscopy was employed to record the evolution of visible reflectance along with color slopes during the exposure of methanol ($^{13}CH_3OH$; 10 and 40 K) and carbon monoxide ($^{13}C^{18}O$; 10 and 20 K) to GCR proxies (Fig. 1) (51, 52). Although only methanol and not yet carbon monoxide was detected on Arrokoth's surface (53), carbon monoxide represents one of the major degradation products of methanol (54, 55). To compare the laboratory studies with New Horizons' data (9), the reflectance spectra (400 to 700 nm) were normalized at 550 nm. Subsequently, the color slopes and colors were extracted as defined in the literature (Fig. 2 and *Methods*) (56–58). At 10 K, reflectance spectra of methanol (Fig. 1*A*) only show a slight change and a color slope of about 13% per 100 nm (Fig. 2*A*). On the contrary, the methanol ices at 40 K and carbon monoxide ices depict noticeable positive shifts of spectral slopes (Fig. 1 *B*–*D*). For methanol irradiated at 40 K, the color slopes initially decrease from 19 to 15% per 100 nm at doses lower than 9.9 eV amu^{-1}. However, as the radiation exposure is extended to 82.1 eV amu^{-1}, the color slopes increase to 32% per 100 nm (Fig. 2*A*). Remarkably, at the dose of about 57 eV amu^{-1}, the color slope can match the mean color slope of Arrokoth, which is about 27% per 100 nm. This indicates that this dose replicates the reddening processing on Arrokoth exceptionally well, spanning at least 1,300 My. The experimental color slopes also replicate the astronomically derived color slopes of cold classic Kuiper Belt objects (CCKBOs) from 18 to 32% per 100 nm. The color-color diagram shows a rising tendency with increasing irradiation time, reproducing that of a population of red and ultrared KBOs similar to Arrokoth. At 10 K, below Arrokoth's surface temperature, the colors match KBOs defined by $B–V \approx 0.82$ to 0.88 and $V–R \approx 0.48$ (Fig. 2*B*). For the carbon monoxide ices, the slopes increase rapidly when the radiation dose reaches 9.9 eV amu^{-1} leveling off at about 35% per 100 nm at 10 K and 12% per 100 nm at 20 K (Fig. 2*C*). The colors of carbon monoxide depict a bimodal distribution depending on the temperature (Fig. 2*D*). At 10 K, the colors mainly occupy $B–V \approx 1.08$ to 1.18 and $V–R \approx 0.52$ to 0.67, matching parts of the ultrared KBOs ($S' \geq 25\%$ per 100 nm), such as (33001) 1997 CU_{29}. However, at 20 K, the colors fall within the neutral regions of $B–V \approx 0.64$ to 0.93 and $V–R \approx 0.35$ to 0.42 and do not correlate with observed KBOs.

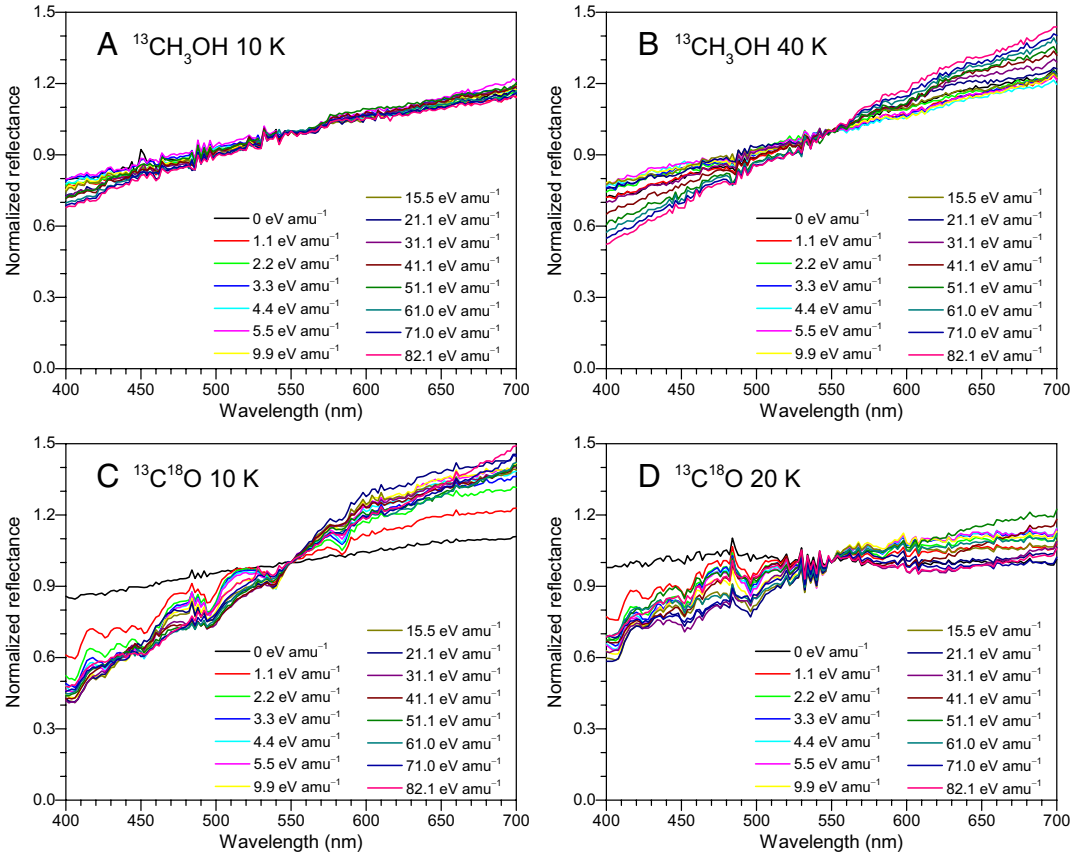

Fig. 1. Visible reflectance spectra normalized at 550 nm collected during the irradiation of methanol ($^{13}CH_3OH$) and carbon monoxide ($^{13}C^{18}O$) ices. (*A*) Spectra of methanol ice irradiated at 10 K, and (*B*) 40 K. (*C*) Spectra of carbon monoxide ice irradiated at 10 K, and (*D*) 20 K.

The color slopes of irradiated ices heated to 320 K were also recorded. This mimics the transport of a KBO from the Kuiper Belt to the inner Solar System as a short-period comet (*SI Appendix*, Figs. S1 and S2). In the methanol system, after irradiation at 10 K, the color slopes reveal no temperature dependence giving a slope of about 15% per 100 nm. However, after irradiation at 40 K, the color slopes decrease from 29 to 19% per 100 nm as the temperature rises to 320 K. These residues exhibit a blue-white appearance, as shown in *SI Appendix*, Fig. S3, and remain stable even after removal from the vacuum chamber for several weeks. For carbon monoxide after irradiation at 10 K, the color slopes decrease from 35% per 100 nm to an asymptotic value of 25% per 100 nm at about 140 K. After irradiation of carbon monoxide at 20 K, the color slopes show a temperature-independent value of about 9% per 100 nm during TPD. These findings suggest that the color slopes of KBOs with species bearing carbon, oxygen, and hydrogen elements will exhibit a negative shift with heating during their journey toward the inner Solar System, supporting the depletion of ultrared matter on observed short-period comets (47).

Altogether, methanol ices processed by GCR proxies at 40 K replicate the color slopes of CCKBOs, and most importantly, Arrokoth. The significant change in color slopes during the irradiation reflects a strong dose dependence on the colors of KBOs covered by carbon, oxygen, and hydrogen-bearing molecules. The average color slope of 27% per 100 nm of Arrokoth replicates the exposure of methanol ice on Arrokoth's surface over a radiation dose of about 57 eV amu^{-1}. This suggests that the surface ices of Arrokoth have been exposed to GCRs for at least 1,300 My. Chemically speaking, this ultrared surface can plausibly be associated with increased conjugated π bond systems in complex organic molecules (59, 60). However, it is not feasible to define specific chromophores from the reflection spectra that lack distinctive features. To identify the nature of the chromophores responsible for the reddish surface of Arrokoth, complementary analytical techniques as described below are required to constrain the chromophores in the exposed methanol and carbon monoxide ices.

FTIR Spectroscopy. The FTIR permits the identification of functional groups, including potential chromophores, in complex mixtures of molecules. The development of these functional groups can be traced over the radiation dose (Fig. 3 and *SI Appendix*, Figs. S4–S10). At 40 K, the pristine methanol ice shows fundamentals of methanol such as the O—H stretching (3,382 to 3,130 cm^{-1}) and ^{13}C—H stretching (2,976 to 2,825 cm^{-1}) (54, 61) (Fig. 3*A* and *SI Appendix*, Table S4). After irradiation, besides functional groups of hydroxyl (O—H) and aliphatic hydrocarbons (^{13}C—H), a set of new absorptions emerges (Fig. 3*B*). Two intense peaks at 2,275 and 2,091 cm^{-1} demonstrate the production of carbon dioxide ($^{13}CO_2$) and carbon monoxide (^{13}CO), respectively, providing an alternative source of carbon dioxide and carbon monoxide recently identified on KBOs by the James Webb Space Telescope (JWST) (62, 63). Since carbon monoxide is volatile at 40 K, the carbon monoxide detected here is likely trapped in a polymer matrix during the irradiation. Weak absorption bands between 1,805 and 1,569 cm^{-1} are assigned to ^{13}C═O and ^{13}C═^{13}C stretching vibrations along with ν_3 mode of $H_2{}^{13}CO$ at 1,496 cm^{-1} and ν_3 mode $^{13}CH_4$ at 1,294 cm^{-1} (Fig. 3*C*). A broad band between 1,300 and 1,000 cm^{-1} can be linked to the overlapping ^{13}C—O stretching and ^{13}C—H bending modes of a large number of synthesized species. The feature between 881 and 828 cm^{-1} can be connected to the ^{13}C—H wagging and ^{13}C—^{13}C—O stretching modes (61). After heating to 320 K, the spectrum of the solid residue reveals O—H and ^{13}C—H stretching bands between

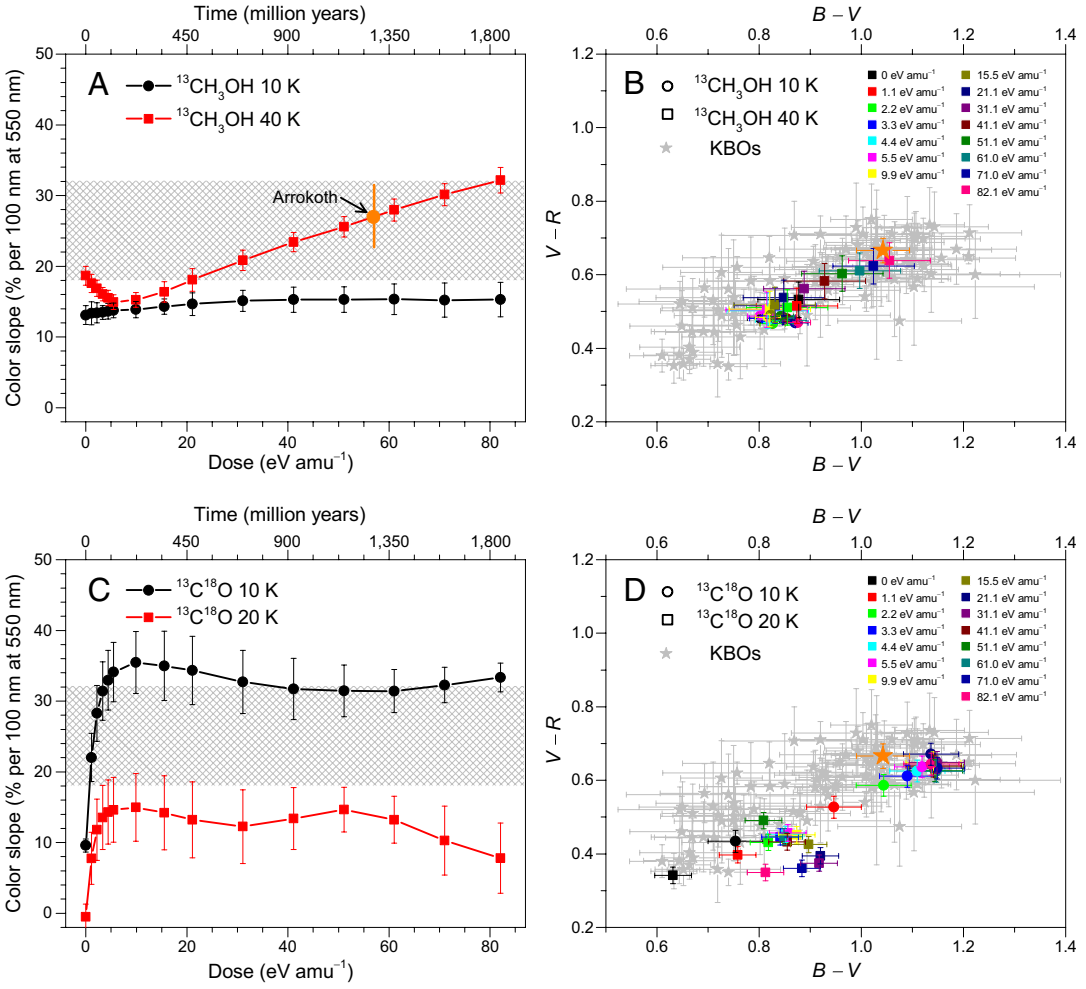

Fig. 2. Comparison of the color between irradiated methanol and carbon monoxide ices with Kuiper Belt objects (KBOs). (*A*) Color slope evolution of irradiated methanol ice and comparison with cold classical Kuiper Belt objects (CCKBOs) and Arrokoth. The gray zone defines the range of CCKBOs' color slopes. The color slope position of Arrokoth indicates its surface has been processed by galactic cosmic rays (GCRs) at a dose of about 57 eV amu^{-1}. Error bars shown are from linear fitting of spectra. (*B*) Comparison of the color between irradiated methanol ice with KBOs; methanol ices irradiated at 10 K are shown with circles and at 40 K coded with squares, dose sequence is coded with different colors. Arrokoth position is marked with an orange star. Error bars shown are 1σ values. (*C*) Color slope evolution of irradiated carbon monoxide ice and comparison with CCKBOs. The gray zone represents the range of CCKBOs' color slope. Error bars shown are from linear fitting of spectra. (*D*) Comparison of the color between irradiated carbon monoxide ice with KBOs; carbon monoxide ices irradiated at 10 K are shown with circles and at 20 K coded with squares, dose sequence is coded with different colors. Arrokoth color is marked with an orange star. Error bars shown are 1σ values.

3,481 and 2,866 cm^{-1} (Fig. 3*D*). The $^{13}C{=}O$, $^{13}C{=}{}^{13}C$, and $^{13}C{-}O$ stretches are also observed between 1,682 and 1,000 cm^{-1}. At 10 K, the spectra of the irradiated methanol reveal similar functional group features compared to those produced by 40 K irradiation (*SI Appendix*, Fig. S4 and Table S5). For the carbon monoxide ices irradiated at 10 K (*SI Appendix*, Fig. S5) and 20 K (*SI Appendix*, Fig. S6), multiple new peaks corresponding to linear carbon-oxide species are detected, which include carbon dioxide ($^{13}C^{18}O_2$), carbon suboxide ($^{13}C_3{}^{18}O_2$), tetracarbon dioxide ($^{13}C_4{}^{18}O_2$), pentacarbon dioxide ($^{13}C_5{}^{18}O_2$), dicarbon monoxide ($^{13}C_2{}^{18}O$), and tricarbon monoxide ($^{13}C_3{}^{18}O$) (*SI Appendix*, Tables S6 and S7) (55). Absorption of the carbonyl $^{13}C{=}{}^{18}O$ group stretching is only detected at 10 K. At 320 K, both conjugated $^{13}C{\equiv}{}^{13}C$ and $^{13}C{=}{}^{18}O$ stretches are observable in the spectrum of carbon monoxide irradiated at 10 K, while conjugated $^{13}C{\equiv}{}^{13}C$ features are detected in the residues from the 20 K irradiation experiment. The lack of the $^{13}C{=}{}^{18}O$ stretching in 20 K experiments indicates that the carbonyl functional group is fundamental in producing the ultrared residues.

Having identified those functional groups produced during irradiation, it is important to trace their evolution during the irradiation, i.e., during the exposure of KBO surfaces in space over time. In the methanol system at 40 K (Fig. 4), the column densities of the reactant decrease as the doses increase, with 94% of methanol being destroyed by the exposure to ionizing radiation (Fig. 4*A*). Simultaneously, the carbon dioxide and carbon monoxide products grow continuously reaching maximum column densities of (4.2 ± 0.4) × 10^{16} and (3.8 ± 0.4) × 10^{16} molecules cm^{-2}, respectively (Fig. 4 *B* and *C*). The formyl radical ($H^{13}\dot{C}O$) rises to (2.0 ± 0.2) × 10^{14} molecules cm^{-2} at a dose of about 5.5 eV amu^{-1} and then flattens out (Fig. 4*D*). Methane column densities increase until about 9.9 eV amu^{-1} followed by a decline due to the competition between synthesis and decomposition to (3.0 ± 0.3) × 10^{15} molecules cm^{-2} (Fig. 4*E*). The end product of the loss of methane can be attributed to the formation of aromatics and/or polyacetylene, as previously reported (64). The integrated areas of the $^{13}C{=}O$ and $^{13}C{=}{}^{13}C$ functional groups reveal monotonic growth profiles (Fig. 4*F*). These trends suggest a multistep degradation of methanol through hydrogen loss (*SI Appendix*, Table S8). Quantitatively speaking, the carbon atoms found in carbon dioxide, carbon monoxide, and methane account for (65 ± 6)% of the carbon atoms in the consumed methanol. Note

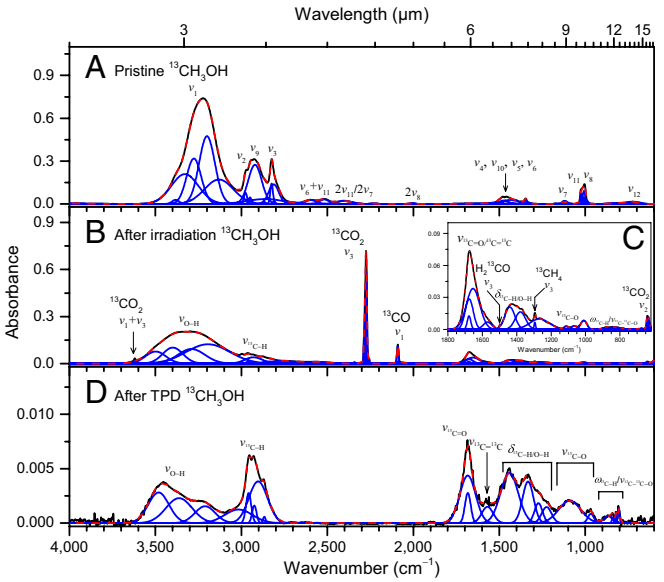

Fig. 3. Deconvoluted FTIR spectra of methanol ice irradiated at 40 K. (*A*) Pristine ices at 40 K. (*B*) After irradiation at 40 K. (*C*) The magnified view of the region 1,800 to 620 cm^{-1} of methanol ice after irradiation at 40 K. (*D*) The residue at 320 K. The experimental spectrum is plotted in black, while the deconvoluted peaks are blue and their sum is shown with the dashed red line. For clarity, only noticeable peaks are labeled, and detailed peak assignments are listed in *SI Appendix*, Table S5.

that the levels of volatile CO and CH_4 trapped in irradiated methanol are higher than those found in previous reports (42, 54). This increase could stem from the high dose accumulation in our experiments, leading to continuous losses of hydrogen and oxygen atoms. The temporal evolution of methanol during irradiation at 10 K also reveals carbon dioxide, carbon monoxide, and methane (*SI Appendix*, Fig. S11). The carbon atoms in these molecules account for (70 ± 7)% of the carbon atoms consumed in methanol. In addition, the methanol experiment at 40 K shows a higher ratio of carbon dioxide to carbon monoxide (*SI Appendix*, Fig. S12). In the carbon monoxide ices (*SI Appendix*, Figs. S13 and S14), the reactants continually decrease during irradiation. The products $^{13}C^{18}O_2$, $^{13}C_3{}^{18}O$, and $^{13}C_3{}^{18}O_2$ demonstrate a rapid increase followed by a decrease to an asymptotic value. At 10 K, the maximum concentrations of $^{13}C^{18}O_2$, $^{13}C_3{}^{18}O$, and $^{13}C_3{}^{18}O_2$ reach to (1.8 ± 0.2) × 10^{16}, (2.3 ± 0.2) × 10^{15}, and (2.7 ± 0.3) × 10^{14} molecules cm^{-2}. At 20 K, these values are (1.2 ± 0.1) × 10^{16}, (1.9 ± 0.2) × 10^{15}, and (1.9 ± 0.2) × 10^{14} molecules cm^{-2}. Carbon dioxide reaches peak values at about 9.9 eV amu^{-1}, lagging behind that of $^{13}C_3{}^{18}O$ and $^{13}C_3{}^{18}O_2$. These patterns imply a consecutive kinetics scheme A ($^{13}C^{18}O$) → B ($^{13}C^{18}O_2$, $^{13}C_3{}^{18}O$, and $^{13}C_3{}^{18}O_2$) → C (carbonaceous compounds) converting carbon monoxide to complex carbonaceous materials through oxygen loss (*SI Appendix*, Table S9) (55, 65).

We also recorded the abundance of molecular hydrogen (H_2) and molecular oxygen (O_2) released from the methanol and carbon monoxide ices, respectively, via a quadrupole mass spectrometry (QMS, *Methods*) during the irradiation and TPD to 320 K. As the radiation dose increased, the hydrogen molecules accumulated to (1.6 ± 0.2) × 10^{13} and (2.6 ± 0.3) × 10^{13} at 10 K and 40 K (*SI Appendix*, Fig. S15*A*). Hydrogen molecules detected during the TPD at 10 K and 40 K are (2.9 ± 0.3) × 10^{15} and (1.0 ± 0.1) × 10^{15}, respectively. The enhanced yield of molecular hydrogen released during TPD reveals that the irradiated methanol can trap molecular hydrogen even at 40 K within the ice matrix. For carbon monoxide, (1.4 ± 0.1) × 10^{10} and (9.3 ± 0.9) × 10^{9} oxygen molecules are released in the irradiation at 10 K and 20 K, respectively

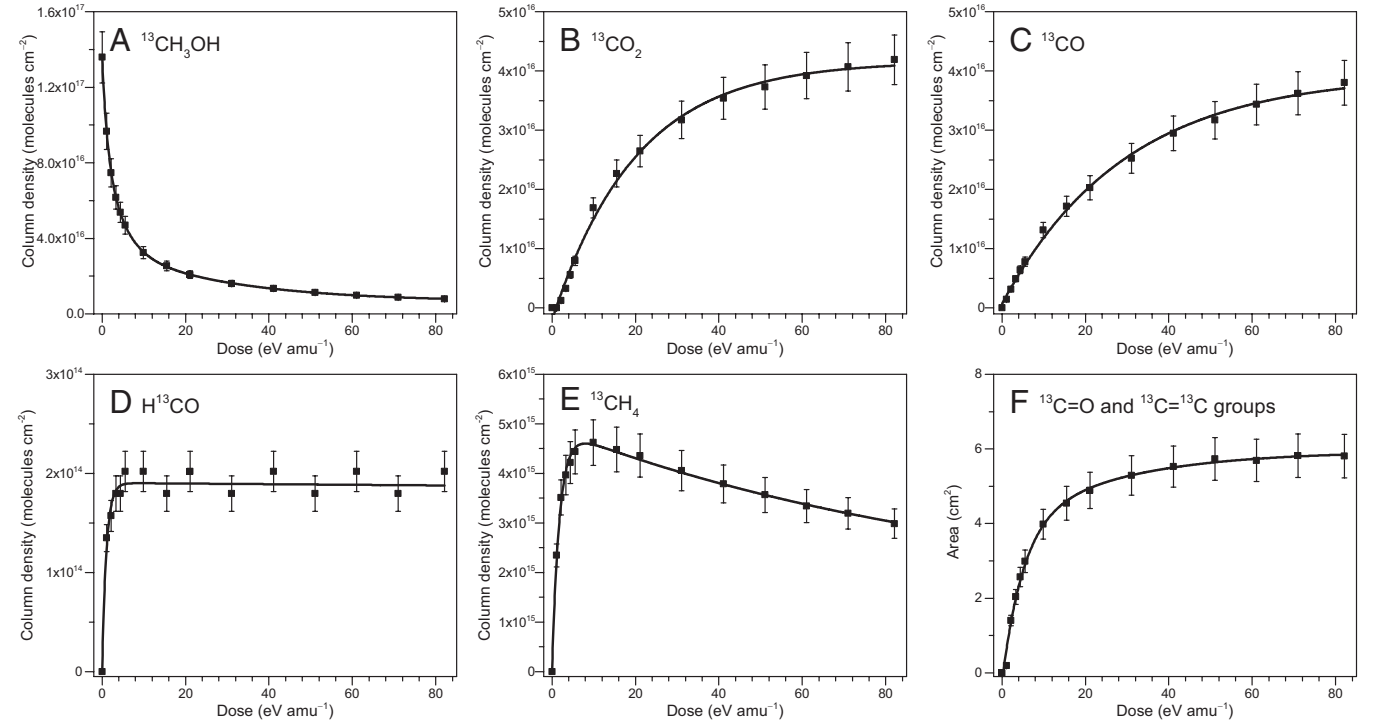

Fig. 4. The evolution and kinetic fits of key species and functional groups during the irradiation of methanol ($^{13}CH_3OH$) ice at 40 K. (*A*) Column densities of methanol ($^{13}CH_3OH$, average of absorptions at 1,124 cm^{-1} and 1,005 cm^{-1}). (*B*) Column densities of carbon dioxide ($^{13}CO_2$, 2,275 cm^{-1}). (*C*) Column densities of carbon monoxide (^{13}CO, 2,091 cm^{-1}). (*D*) Column densities of formyl radical ($H^{13}\dot{C}O$, 1,805 cm^{-1}). (*E*) Column densities of methane ($^{13}CH_4$, 1,294 cm^{-1}). (*F*) Area of ^{13}C=O and ^{13}C=^{13}C stretching modes (integrated between 1,520 and 1,790 cm^{-1}). Note that, both ^{13}CO and $^{13}CH_4$ are volatile at 40 K and they are likely trapped within the polymer matrix formed from processed methanol ice. All the error bars are ±10% of the corresponding column densities and areas. Rate constants derived from the kinetic fitting and corresponding chemical reaction scheme are compiled in *SI Appendix*, Table S8.

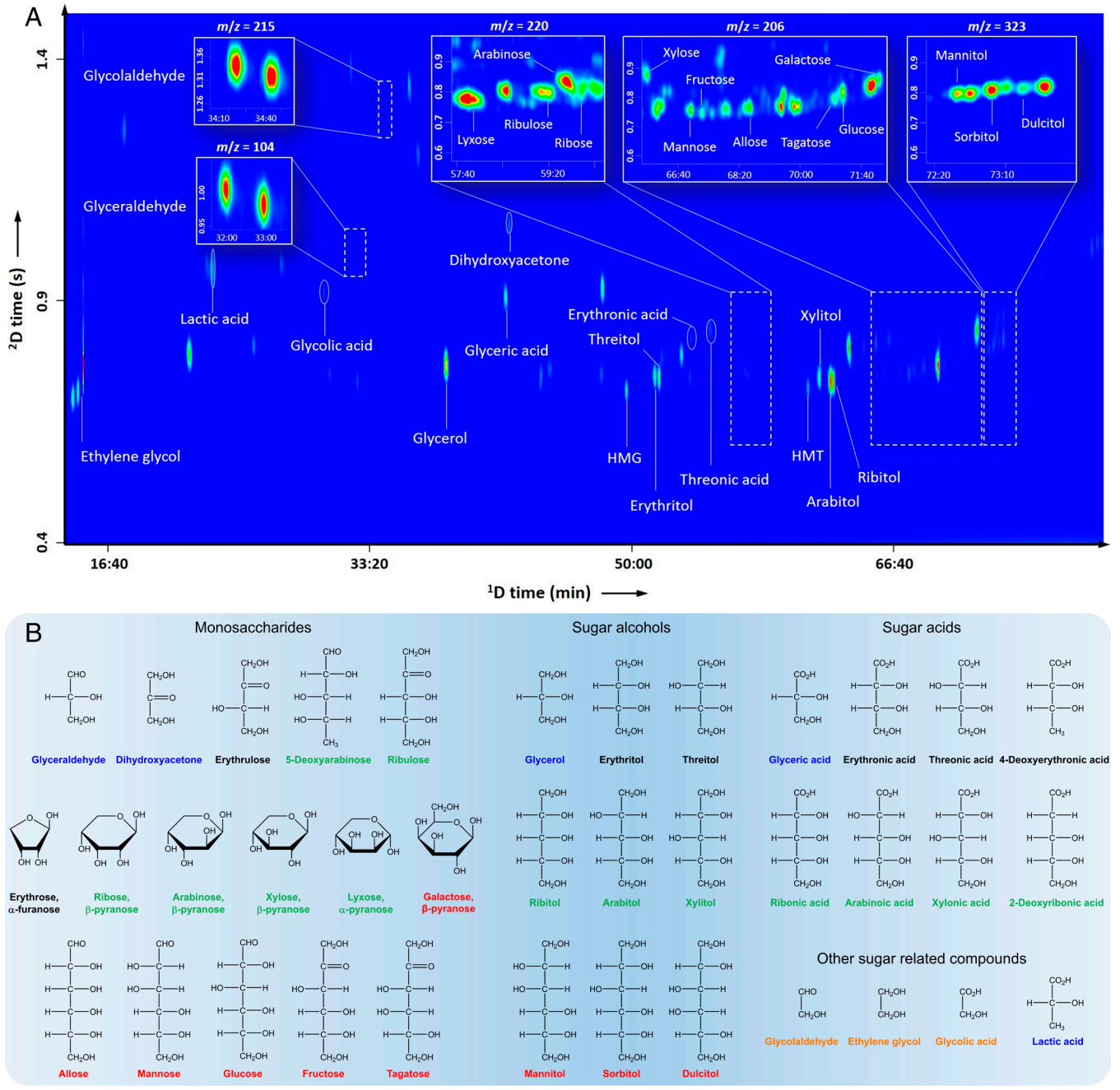

Fig. 5. Sugars and related compounds detected in the residue of methanol ices irradiated at 40 K by two-dimensional gas chromatography along with their detailed structure. (*A*) Sugar and related compounds detected as BSTFA derivatives in the irradiated methanol residue resolved on a Chirasil-Dex column in the first dimension coupled to a DB Wax in the second dimension. Mass-to-charge ratios (*m/z*) 104, 193, 206, 215, 220, 294, and 323 are displayed. ^{1}D and ^{2}D represent the first-dimension and second-dimension times of the columns, respectively. (*B*) Detailed structures are identified in the residues by means of two-dimensional gas chromatography. Structures of the chiral molecules represent the D-enantiomer. Names of molecules are color-coded according to the number of carbon atoms: two carbon atoms (C2) orange, C3 blue, C4 black, C5 green, and C6 red. The quantities of 23 molecules are given in *SI Appendix*, Table S10.

(*SI Appendix*, Fig. S15*B*). Similar to methanol, $(3.4 \pm 0.3) \times 10^{12}$ and $(1.6 \pm 0.2) \times 10^{11}$ oxygen molecules are trapped in the ice at 10 K and 20 K, respectively, which are released during the TPD. The sequestration of molecular hydrogen and oxygen within irradiated methanol and carbon monoxide ices is an important finding since pure hydrogen cannot be condensed at 10 K; likewise, neat molecular oxygen sublimes at 25 K (66). In addition, the findings suggest that more molecules were detected during TPD phase, as compared to the irradiation stage. This indicates that the majority of these two products are trapped within the processed matrices. Altogether, the UV-vis reflectance spectra of irradiated methanol at 40 K show a trend of increasing color slopes and replicate that value of Arrokoth. FTIR spectroscopy shows the increase of $^{13}C{=}O$ and $^{13}C{=}{}^{13}C$ functional groups, in which conjugated $^{13}C{=}O$ and $^{13}C{=}{}^{13}C$ are potential chromophores for the products to induce the reddening of irradiated methanol ices. However, since FTIR spectroscopy can only identify functional groups of a complex mixture of compounds, additional analytical tools are required to identify individual species.

Two-Dimensional Gas Chromatography Time-of-Flight Mass Spectrometry. The residues remaining after GCR proxy processing of the methanol ices and heating to 320 K were analyzed via GC×GC–TOF-MS (*Methods*) (67). Utilizing ^{13}C—labeled methanol in the

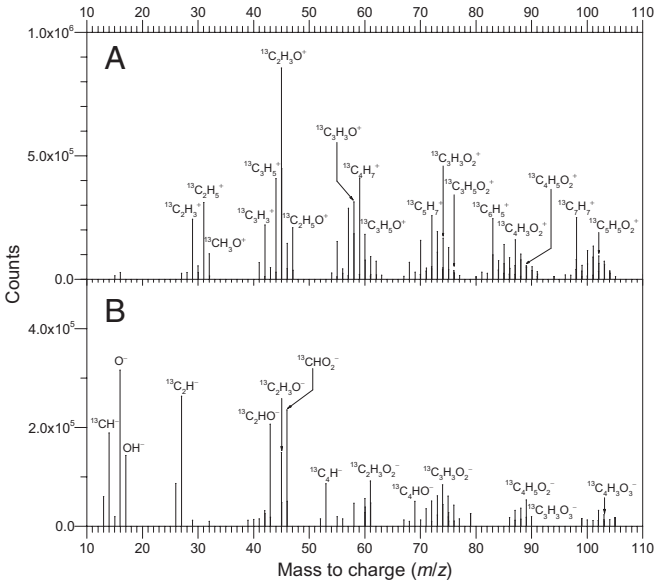

Fig. 6. Secondary ion mass spectra from residues of methanol ($^{13}CH_3OH$) ices irradiated at 40 K with a radiation dose of 8.8 eV amu^{-1}. The mass spectra were recorded in (*A*) positive and (*B*) negative ion detection modes. For clarity, only sugars and sugar-related fragments are labeled. Detailed mass spectra obtained from irradiated methanol ices by higher doses can be found in *SI Appendix*, Figs. S16 and S18.

irradiation experiments, the fully ^{13}C—labeled products identified here originate from the radiation exposure of the methanol ices at temperatures similar to those of the Kuiper Belt. The GC×GC–TOF-MS data unveiled a series of biologically important monosaccharides, sugar alcohols, sugar acids, and hydroxycarboxylic acid (Fig. 5*A*). Monosaccharides containing six carbon atoms (denoted C6), including galactose, allose, mannose, glucose, fructose, and tagatose were identified in processed methanol ices. Among them, glucose represents the most significant source of energy for metabolism in living organisms. Furthermore, fundamental molecules integral to contemporary biochemistry on Earth, such as ribose, define key components of RNA. The backbone molecule of lipids—glycerol—was also observed in the residues. These sugars and their derivatives are generated via nonequilibrium chemical processes triggered by GCRs proxies and provide a complex suite of sugar and related molecules similar to the UV photolysis of methanol-bearing ice mixtures (20–22).

Some 40 monosaccharides and derivatives were identified (Fig. 5*B*), of which 23 species were sufficiently resolved for a quantitative analysis (*SI Appendix*, Table S10). For the 1.1 eV amu^{-1} system, the most abundant monosaccharides are C3 compounds (glyceraldehyde and dihydroxyacetone), followed by sugars of C6 (galactose, allose, and tagatose), C5 (arabinose, ribose, and xylose), and C4 (erythrose and erythrulose). The molecular complexity of the sugar-containing residues prevented the quantification of all structural isomers of aldoses and ketoses based on the number of carbon atoms in the main chain. A comprehensive quantitative comparison of potential reaction pathways for aldose and ketose sugars, contingent upon chain length, is therefore unattainable. However, it is unlikely that sugars could have been formed through a simple stepwise elongation process, i.e., C4 formation from C3, C5 formation from C4, and C6 formation from C5. This is because such a process would lead to a decrease in mass from C3 to C6, a trend that was not observed in our experiments, despite our limited quantitative data. Alternatively, for example, C6 sugars could be formed from C3 sugar precursors, which would bypass the sequential chain elongation for the production of larger sugars. Altogether, the well-resolved sugars and their derivatives accumulated up to 4.2×10^{-8} g with a conversion efficiency of about 0.06 ± 0.01% with respect to the processed methanol reactants over 24 My in the Kuiper Belt. This should be considered as the minimum quantity of sugars present, as additional structural isomers have been detected or may coelute, but their identification and quantification was impeded by the samples' complexity. For the current age of our Solar System—under the premise that a fresh methanol surface is provided through resurfacing—this would translate to a minimum conversion rate of 11.5 ± 2.5%. Based on this potentially high conversion efficiency, a large amount of sugar is expected on its surface thus dubbing Arrokoth a sugar world. These carbohydrates and their derivatives serve as precursors for fundamental biological molecules such as RNA and lipids. They offer a unique opportunity and plausible source of prebiotic molecules to be delivered to early Earth from the Kuiper Belt in the form of short-period comets. Although GC×GC-TOF-MS provides compelling evidence of sugar and derivatives resulting from irradiated methanol under Kuiper Belt environments, gas chromatography can only analyze the soluble residue. Further studies are required to untangle the chemical composition of the remaining insoluble residues.

Time-of-Flight Secondary Ion Mass Spectrometry. The insoluble fractions of the residues were analyzed via TOF-SIMS. This technique bombards the samples with energetic ions of Bi_3^+ and sputters cationic and ionic fragments of the molecules embedded in the residue surface. These fragments are specific to molecular building blocks of organics in the insoluble residue and can be used to aid in the identification of species present (68). The TOF-SIMS analysis suggests multiple cation and anion fragments of monosaccharides with mass-to-charge (m/z) ratios of up to 110 such as the cations $^{13}C_2H_3O^+$, $^{13}C_3H_3O^+$, and $^{13}C_3H_3O_2^+$ and anions $^{13}C_2H_3O^-$, $^{13}CHO_2^-$, and $^{13}C_3H_3O_2^-$ (Fig. 6) (69, 70). These fragments can also originate from the polysaccharides resulting from the condensation reaction of monosaccharides such as glycogen (71). Besides the fragments of sugars and their derivatives, various moieties of PAHs were also observed in the positive ion mode (*SI Appendix*, Fig. S16 and Table S11) (72). These PAH units carry up to six benzene rings such as yellowish anthanthrene ($^{13}C_{22}H_{12}$) and may undergo further molecular mass growth processes to form more complex PAHs, e.g., reddish ovalene ($^{13}C_{32}H_{14}$), thus making contributions to Arrokoth's reddish appearance (73). Two processes can contribute to the formation of PAHs. The first is that PAHs originate from sugars and their derivatives. During extended periods of the accumulation of radiation doses, a decline in the concentration of sugars and their derivatives is observed, while the levels of PAHs increase. This trend supports the pathway converting sugar and related compounds to PAHs (*SI Appendix*, Fig. S17). An alternative process generating PAHs occurs when ionizing radiation interacts with methane (64). Methane is a primary decomposition product of irradiated methanol and can be trapped within the ice matrix at 40 K. In addition, highly unsaturated hydrogen-terminated carbon chains are observed in the negative ion spectra of the methanol residues. These fragments were also identified in both the positive and negative ion modes of the residues of the processed carbon monoxide ices (*SI Appendix*, Figs. S18 and S19 and Tables S12–S14). These unsaturated carbon chain moieties can serve as linkers connecting sugars; these linkers in particular can connect aromatics moieties and their derivatives to expand the conjugated π bonds system, subsequently leading to positive

shifts in the color slope of optical spectra during the irradiation of Arrokoth model ices.

Discussion

The New Horizons flyby of the Kuiper Belt object (486958) Arrokoth revealed a reddish surface with a high color slope of 27% per 100 nm accompanied by a coating of methanol-containing ices. The present study combines laboratory experiments on the radiation exposure of Arrokoth's methanol ices by GCR proxies merged with in situ spectroscopic (FTIR and UV-vis) and ex-situ analyses (GC×GC–TOF-MS and TOF-SIMS) of the ices and residues. It thus provides insights into the underlying physical and chemical processes responsible for the surface reddening of Arrokoth. These laboratory simulation experiments offer compelling evidence of radiation-induced reddening of methanol ices, mimicking geological time scales of up to approximately 1,800 My in the Kuiper Belt. The excellent alignment between the color slopes of Arrokoth and irradiated methanol suggests that Arrokoth's surface has been exposed to radiation from GCRs for at least 1,300 My excluding resurfacing events such as collisions between KBOs, which can also alter their surface colors (74). The ionization radiation impacting the methanol ices replicates the colors of a population of CCKBOs defined in the range of $B–V \approx 0.87$ to 1.13 and $V–R \approx 0.49$ to 0.69, such as Makemake, Chaos, and Quaoar. Besides its detection on Arrokoth, methanol has also been detected on the surface of 2002 VE_{95} characterized by colors of $B–V = 1.08 \pm 0.03$ and $V–R = 0.71 \pm 0.02$ matching those of irradiated methanol (75). Furthermore, the radiation-induced reddening of the spectra of carbon monoxide—the most abundant diatomic product of methanol radiolysis—is consistent with the recent observations by the James Webb Space Telescope (JWST) that the reddest Trans-Neptunian objects (TNOs) commonly contain carbon monoxide (62).

This study reveals the crucial role of GCR radiation on methanol ice at 40 K in producing ultrared matter on the surfaces of methanol-rich KBOs, particularly, Arrokoth. This exposure results in the formation of a suite of sugar and related molecules previously undetected in any KBO simulation experiment. Recently, Quirico et al. employed high-energy heavy ions including $^{136}Xe^{19+}$, $^{58}Ni^{9+}$, and $^{18}O^{6+}$, with a maximum dose of 5.9 eV amu^{-1} to irradiate methanol ice. Their work revealed a wide variety of products containing olefinic, acetylenic, and carbonyl groups (30). At room temperature, these products exhibit a reddish appearance and show continuous absorption from about 500 nm when dissolved in methanol. However, the color evolution of processed ices at low temperatures, such as those observed on KBOs, has remained ambiguous and was not explained in Quirico et al.'s study. The increasing color slopes observed for methanol processed at 40 K in our study are consistent with the reddening observed in the visible and near-infrared spectra for methanol irradiated at 50 K (38). However, when methanol is irradiated at 120 K, the processed methanol exhibits almost no change, similar to our result with methanol at 10 K. In addition, Sakakibara et al. utilized nitrogen-containing cryoplasma interacting with methanol-water ice mixtures and observed reddish products at 85 K. And the reddish appearance disappeared at temperatures between 120 and 150 K (15), adding complexity to the explanation for the stability of reddish products from methanol ices. Furthermore, Kuiper Belt conditions can be more complex than any simulation experiment worldwide. Not only can radiation conditions, such as different ice compositions, temperature, and dose accumulation alter the surface color of KBOs (48), but dynamical processes such as randomized collisional excavation (31), velocity-dependent impact resurfacing (32), and fall-back debris condensation from comet-like activity (76) can also influence the evolution of KBO surfaces. The color diversity of KBOs was initially attributed to the interplays between the reddening effect caused by irradiation on fresh icy surfaces and the resurfacing processes such as impacts, which tend to decrease the reddening (74). Notably, the impact crater density model suggests that the surface age of Arrokoth exceeds 4 billion years (8) and is accompanied by processes that decrease the reddening of its surface. Considering this, it is expected that 4 billion years of GCR radiation exposure to methanol ice should result in a higher color slope than what is currently on Arrokoth, as indicated by the trend of color slopes shown in Fig. 2*A*.

On the molecular level, the GC×GC–TOF-MS and TOF-SIMS results provide compelling evidence for the formation of sugars and their derivatives carrying up to six carbon atoms, such as glucose and allose, in the irradiated methanol ices. Ribose—the contemporary biomolecular building block of RNA—is also identified in pure methanol ices, implying the existence of these C5 sugars on Arrokoth. On the other hand, varieties of PAH motifs carrying up to six rings such as naphthalene ($^{13}C_{10}H_8$), pyrene ($^{13}C_{16}H_{10}$), and anthanthrene ($^{13}C_{22}H_{12}$) were also observed. These PAHs and their derivatives might be linked by highly unsaturated carbon chains or undergo further molecular mass growth processes to form more complex macromolecules extending conjugated π systems as essential makers for the reddish appearance of Arrokoth (64). The formation of abundant sugar and related molecules dubs Arrokoth as an intriguing sugar world in the outer Solar System. Since KBOs have been suggested as main source of short-period comets, these sugars and their derivatives could have been delivered by KBOs like Arrokoth in the form of short-period comets impacting the early Earth, thus providing a source of a variety of sugars and the feedstock for important biomolecules such as RNA.

While this study primarily focuses on Arrokoth, the aforementioned results can be extended to unravel the physical and chemical properties of KBOs, whose surfaces contain carbon, oxygen, and hydrogen along with the carbon monoxide-rich interstellar comet 2I/Borisov (77). In addition, water and ammonia have been detected in a population of KBOs such as Charon and Orcus (11). Carbon dioxide was also recently identified on KBO surfaces by the JWST (62, 63). Further experiments are warranted to probe ice mixtures carrying ammonia, water, and carbon dioxide to gauge their impact on the chemistry, such as the inventory of biorelevant molecules that can be synthesized and their effect on the optical spectra. This approach will eventually replicate the color diversity of KBO surfaces and untangle key chromophores on the molecular level. Exposure of ices to combined GCR and solar wind proxies accompanied by simulated resurfacing is desirable to explore their cumulative effects on the chemical processing of KBO surfaces. These synergistic effects are expected to develop the concepts of how complex organic molecules could have been synthesized in the outer Solar System, ultimately leading to a better understanding of the origin and evolution of our Solar System.

Methods

Irradiation Experiments. The irradiation experiments were performed in an ultrahigh vacuum (UHV) chamber at a pressure of about 10^{-11} Torr (51, 52) and the experimental setup has been described in detail elsewhere (64). Briefly, a polished silver wafer coated with rhodium is attached to an oxygen-free high conductivity (OFHC) copper cryostat via indium foil and connected to a two-stage closed-cycle helium refrigerator (CTI-Cryogenics Cryodyne 1020, compressor: CTI-Cryogenics 9600). The temperature of silver wafer is monitored by a silicon diode sensor (Lakeshore DT-470) and regulated in a range of 5 to

320 K with a precision of ±0.3 K by a programmable temperature controller (Lakeshore 336). When the substrate is cooled to 10, 20, and 40 K, methanol ($^{13}CH_3OH$, Sigma Aldrich, >99.9%), and carbon monoxide ($^{13}C^{18}O$, Sigma Aldrich, >99.9%) are deposited onto the wafer via a glass capillary array. Here, we use 13−carbon labeled reactants to eliminate any potential contaminants. Based on the refractive index (n) of 1.33 ± 0.04 for solid methanol and of 1.25 ± 0.03 for carbon monoxide (78), the thicknesses of the ices are calculated to be 800 ± 50 nm (79).

After deposition, the methanol and carbon monoxide ices are isothermally processed by 5 keV electrons (Specs EQ 22 to 35 electron source) simulating secondary electrons formed in the track of galactic cosmic rays (GCRs) penetrating the ices. The electron incidence angle is 70° to the ice surface normal. Utilizing Monte Carlo simulations (CASINO 2.42) (80), the average depths of the electrons are estimated to be 230 ± 30 nm for methanol and 270 ± 30 nm for carbon monoxide. The maximum depths of the electron penetration are estimated to be 550 ± 50 nm, which is less than the ice thickness of 800 ± 50 nm thus avoiding interaction between the electrons and the coated rhodium surface. The electrons were calculated to deposit average doses of 82.1 ± 10 eV amu^{-1} into methanol and carbon monoxide ice (*SI Appendix*, Table S2). To enable the comparison between our results and the dose accumulation in the outer Solar System, we provide the unit of the deposited dose in eV amu^{-1}, which is widely adopted in the astronomy community (30, 81, 82). This unit can be converted to eV molecule^{-1} used in the astrochemistry community by multiplying the units of eV amu^{-1} by the molecular mass of the reactants, i.e., 28 amu molecule^{-1} for carbon monoxide and 32 amu molecule^{-1} for methanol. It is noteworthy that objects in the Kuiper Belt undergo continuous exposure to ionizing radiation including ultraviolet (UV) photons and charged particles originating from solar winds and galactic cosmic rays (GCRs) (48, 83). Among those sources of ionizing radiation, charged particles consist of more than 90% protons (H^+) and 1 – 10% Helium nuclei (He^{2+}), with solar wind particles typically having energies in the range of a few keV and GCR particles reaching energies in the hundreds of MeV (84, 85). The UV radiation exhibits a flux of about 10^3 photons cm^{-2} s^{-1} with energies lower than 20.0 eV (86). The chemistry of KBO surfaces is predominantly controlled by secondary electrons, generated by ionizing radiation penetrating ices. Essentially, implanted protons transfer their kinetic energy to the electronic system of target molecules, leading to the generation of electrons with energies up to a few keV (43, 87). The electronic linear energy transfer (LET) of MeV protons to molecules within such ices exhibits a similar value of a few keV μm^{-1} as the 5 keV electrons used in the present experiments (88). Our laboratory experiments mimic the formation of reddish materials in methanol and carbon monoxide matrices through charged particles via electronic energy-loss processes on KBO surfaces at low temperatures. In addition, previous research has shown that radiation products from interstellar ices are weakly dependent on the type of irradiation whether electrons, heavy ions, or UV photons (89–92).

Upon completion of irradiation, temperature-programmed desorption (TPD) studies were carried out by heating the substrate to 320 K at a rate of 1 K min^{-1}. The methanol and carbon monoxide ices were analyzed in situ by an UV–vis spectrometer (Thermo Scientific Evolution 300) and FTIR spectrometer (Nicolet 6700). The FTIR spectrometer was operated in absorption-reflection-absorption mode at a reflection angle of 45° and monitored the infrared region of 6,000 to 500 cm^{-1}, using a resolution of 4 cm^{-1}. Simultaneously, the focused light of the UV–vis spectrometer was reflected from the rhodium-coated silver wafer at an angle of 30° and focused onto a photodiode shielded from ambient light. The reflectance spectra in the range of 190 to 1,100 nm were recorded with a resolution of 4 nm. FTIR analyses allowed for the vibrational modes of the reactants and products to be monitored while UV–vis probed the electronic transitions present. In addition, mass spectra of the gas phase species were recorded using a quadrupole mass spectrometer (QMS) operating in the residual-gas-analyzer (RGA) mode with an electron impact ionization energy of 70 eV. In some cases, the reflectance spectra of UV–vis are superimposed by strong interference features since the thickness and refractive index of the films slightly changed during the irradiation, and a simple subtraction of the two spectra cannot be applied to remove the interference bands. To obtain experimental UV−vis spectra free from interference patterns, the interference was derived theoretically by employing a "two interfaces between three media" model generalized for complex refractive indices $n_i + ik_i$(93). To compare UV−vis reflectance spectra measured here with astronomical observations, the visible range of the reflectance spectra (400 to 700 nm) was normalized with respect to the reflectance at 550 nm. The color slopes S' (% per 100 nm) were calculated through Eq. **1** as below defined in the literature (44) with reflectance R of the spectrum at the wavelength λ (nm).

$$S' = \frac{dR/d\lambda}{R_{550\,nm}} \times 100\,\% \times 100\ \text{nm}. \quad [\mathbf{1}]$$

Besides the color slopes, we also computed the color which is defined as the difference in magnitude of radiant flux (logarithmic scale) between two different filters in astronomy. For the spectrum of an astronomical object, the color is determined via Eq. **2** (44),

$$B - V = (B-V)_{Sun} + 2.51\ log\left(\frac{2 + S\Delta\lambda}{2 - S\Delta\lambda}\right), \quad [\mathbf{2}]$$

where $B−V$ is the color of the astronomical object through B- and V-filters, $(B−V)_{Sun}$ is the reference color of the Sun, and $\Delta\lambda$ is the difference between the central wavelengths of the B- and V-filters, with filter ranges of 390 to 510 nm (B) and 490 to 590 nm (V). The V–R color through V- and R-filters with wavelength ranges 490 to 590 nm (V) and 590 to 710 nm (R) were also calculated. To analyze and assign the peaks generated during the irradiation of methanol ices, we deconvoluted its FTIR spectra via the *Fityk* program (Fig. 3 and *SI Appendix*, Figs. S4–S10 and Tables S4–S7). Furthermore, to quantitatively determine the temporal evolution of the identified species and functional group during the irradiation, we integrated key absorption features and estimated their column densities, i.e., the numbers of absorbing molecules per cm^2, N, through a modified Lambert-Beer relationship (94). The absorption coefficients used here are listed in *SI Appendix*, Table S3. Note that, for the newly formed $^{13}C{=}O$ and $^{13}C{=}{}^{13}C$ groups, we could not assign them to any specific species therefore no absorption coefficients can be used. We only plot the evolution of the integrated area from FTIR spectra. The column densities and integrated area of the species and functional group produced by irradiation were fitted by using a kinetic model. The reaction scheme and underlying rate constants for irradiated methanol and carbon monoxide ice were compiled in *SI Appendix*, Tables S8 and S9. The resulting kinetic fits to the column densities of each species and functional group are shown in Fig. 4 and *SI Appendix*, Figs. S11–S14. For the quantification of molecular hydrogen and oxygen outgassing during the irradiation of methanol and carbon monoxide ice, an Extrel 5221 quadrupole mass spectrometer (QMS) operated in the residual-gas-analyzer (RGA) mode with an electron impact ionization energy of 70 eV at a 2 mA emission current was exploited. The secondary electron multiplier was operated at 1,200 V for methanol and carbon monoxide ices. Since the QMS signal is an amplified current generated from the ions, it is necessary to determine the proportionality constant (K) between the number of hydrogen and oxygen molecules (n) in the gas phase and the QMS signal recorded (A). Following the procedure as detailed in the literature (94), these constants were derived to $K_{H2} = (1.4 \pm 0.2) \times 10^8$ molecules counts^{-1} and $K_{02} = (4.2 \pm 0.4) \times 10^4$ molecules count^{-1}. The number of hydrogen and oxygen molecules is then extracted through

$$n = K \int_0^t A\ dt, \quad [\mathbf{3}]$$

where $\int_0^t A\ dt$ are the integrated counts of hydrogen and oxygen QMS signals recorded during the irradiation of methanol and carbon monoxide ices.

Two-Dimensional Gas Chromatography Time-of-Flight Mass Spectrometry.

Sample extraction. Samples were extracted by repeating 10 times the following procedure: 50 μL of MilliQ were spread around the silver wafer surface several times using a micropipette and transferred to a 1 mL Reacti-Vial™. The 500 μL of MilliQ recovered in the vials after extraction were fully dried under a gentle stream of N_2 for about 2.5 h.

Derivatization. For derivatization, 25 μL of pyridine followed by 10 μL of BSTFA reagent were added to the Reacti-Vial™, mixed with a vortex, and heated for 2 h at 80 °C. The mixture was then cooled down for 10 min and dried under a gentle stream of N_2 until approx. 1 μL of the solvent remained, to avoid potential loss of volatile derivatives. Finally, 30 μL of 10^{-6} M methyl laurate (internal standard) in hexane was added, mixed, and transferred to a GC vial for analysis.

GC×GC-TOF-MS instrumentation. The analyses were carried out with a GC×GC Pegasus BT 4D instrument coupled to a reflectron time-of-flight mass spectrometer (LECO) equipped with a dual-stage thermal jet modulator. The GC×GC column configuration consisted of a CP-Chirasil-Dex CB primary column [29.9 m × 0.25 mm inner diameter (ID), 0.25 μm film thickness, Agilent Technologies] coupled to a DB-WAX secondary column (1.41 m × 0.1 mm ID, 0.1 μm film thickness, Agilent Technologies). Hydrogen was used as carrier gas at a constant flow rate of 1.2 mL min^{-1}. Sample volumes of 1 μL were injected in splitless mode at an injector temperature of 230 °C. The primary oven operated as follows: 40 °C for 1 min, the temperature increase of 10 °C min^{-1} to 80 °C and held for 15 min, followed by 2 °C min^{-1} to 180 °C, and an isothermal hold at 180 °C for 15 min. The secondary oven and modulator used the same temperature program with a constant temperature offset of 5 °C and 15 °C, respectively. A modulation period of 3 s was applied. The TOF-MS operated at a storage rate of 150 Hz, with a 50 to 500 amu mass range. Data were acquired and processed with LECO Corp. ChromaTOF™ software.

Calibration curve. In total, 43 compounds were identified in the samples: 38 based on ^{12}C reference standards and five based on literature data. Due to the complexity of the chromatograms, only 23 of the 38 compounds for which standards were available had sufficiently good resolution and stability for absolute quantitative analysis. Calibration curves were prepared for these compounds as the average of two different derivatized mixtures at four different concentrations, injected twice. Linearity was investigated for the following concentrations: 5×10^{-8} M (50 nM), 5×10^{-7} M (500 nM), 5×10^{-6} M (5 μM) and 10^{-5} M (10 μM). Errors (determined as $s/\bar{x} \times 100$) ranged between 5% and 25%, depending on the concentration and the compound analyzed.

Time-of-flight secondary ion mass spectrometry. The insoluble residues were analyzed using a time-of-flight secondary ion mass spectrometry instrument (TOF-SIMS 5-300, ION-TOF) equipped with a reflectron mass analyzer, a 30 keV Bi_n liquid metal primary ion source (Bi-LMIG), and a low-energy electron flood gun. Spectra were acquired with Bi_3^+ in bunched mode with a focus of 2 to 3 mm, a beam current of 0.25 pA, and a total dose of 1.25×10^8 ions. Data were acquired from a 500 μm^2 analysis area. The positive and negative ions from the sputtered residue were recorded, and the mass spectra from TOF-SIMS were analyzed. It is necessary to mention that there are thousands of peaks in the mass spectra, which is similar to a previous report of ions interacting with methanol ice (30), and we only tried to assign the prominent signals in the spectra. Here, we employed a Python code to filter noise and potentially weak and hence ambiguous peaks. The code adds counts in the vicinity *dx* of $^{13}C_xH_yO_z$ masses for the mass to charge (*m/z*) in the range of 0 to 800 amu, where *dx* is M/4,000 determined by the resolution of the mass spectrometer. The vertical cutoff is 10,000 counts, i.e., mass channels with less than 10,000 counts are not shown in the spectra to present the dominant species detected.

Data, Materials, and Software Availability. All study data are included in the article and/or *SI Appendix*.

ACKNOWLEDGMENTS. This study was supported by the U.S. NASA under Grant No. 80NSSC21K1834 and the European Research Council under the European Union's Framework Program for Research and Innovation HORIZON 2020 under Grant ERC 804144.

Author affiliations: [a]Department of Chemistry, University of Hawaii at Mānoa, Honolulu, HI 96822; [b]W.M. Keck Laboratory in Astrochemistry, University of Hawaii at Mānoa, Honolulu, HI 96822; [c]Université Côte d'Azur, Institut de Chimie de Nice, UMR 7272 CNRS, 06108 Nice, France; and [d]Department of Space Studies, Southwest Research Institute, Boulder, CO 80302

1. D. Jewitt, J. Luu, Discovery of the candidate Kuiper belt object 1992 QB_1. *Nature* **362**, 730–732 (1993).
2. D. K. Prialnik, A. Barucci, L. Young, *The Trans-Neptunian Solar System* (Elsevier, ed. 1, 2020), 10.1016/b978-0-12-816490-7.09990-2, p. 478.
3. S. A. Stern, H. A. Weaver, J. R. Spencer, H. A. Elliott, The New Horizons Kuiper belt extended mission. *Space Sci. Rev.* **214**, 77 (2018).
4. S. A. Stern *et al.*, The Pluto system: Initial results from its exploration by New Horizons. *Science* **350**, aad1815 (2015).
5. G. R. Gladstone *et al.*, The atmosphere of Pluto as observed by New Horizons. *Science* **351**, aad8866 (2016).
6. C. B. Olkin, K. Ennico, J. Spencer, The Pluto system after the New Horizons flyby. *Nat. Astron.* **1**, 663–670 (2017).
7. S. A. Stern *et al.*, Initial results from the New Horizons exploration of 2014 MU_{69}, a small Kuiper Belt object. *Science* **364**, eaaw9771 (2019).
8. J. R. Spencer *et al.*, The geology and geophysics of Kuiper Belt object (486958) Arrokoth. *Science* **367**, eaay3999 (2020).
9. W. M. Grundy *et al.*, Color, composition, and thermal environment of Kuiper Belt object (486958) Arrokoth. *Science* **367**, eaay3705 (2020).
10. W. B. McKinnon *et al.*, The solar nebula origin of (486958) Arrokoth, a primordial contact binary in the Kuiper Belt. *Science* **367**, eaay6620 (2020).
11. M. E. Brown, The compositions of Kuiper belt objects. *Annu. Rev. Earth Planet. Sci.* **40**, 467–494 (2012).
12. D. C. Jewitt, J. X. Luu, Colors and spectra of Kuiper belt objects. *Astrophys. J.* **122**, 2099–2114 (2001).
13. M. A. Barucci, F. Merlin, E. Dotto, A. Doressoundiram, C. de Bergh, TNO surface ices. Observations of the TNO 55638 (2002 VE95) and analysis of the population's spectral properties. *Astron. Astrophys.***455**, 725—730 (2006).
14. I. Wong, M. E. Brown, The bimodal color distribution of small Kuiper belt objects. *Astron. J.* **153**, 145 (2017).
15. N. Sakakibara, P. Y. Yu, T. Ito, K. Terashima, Cryogenic-specific reddish coloration by cryoplasma: New explanation for color diversity of outer solar system objects. *Astrophys. J.* **891**, L44 (2020).
16. L. E. Buchanan *et al.*, Col-OSSOS: Probing Ice Line/Color Transitions within the Kuiper Belt's Progenitor Populations. *Planet. Sci. J.* **3**, 9 (2022).
17. S. D. Benecchi *et al.*, The color and binarity of (486958) 2014 MU69 and other long-range New Horizons Kuiper Belt targets. *Icarus* **334**, 22–29 (2019).
18. L. F. Coelho *et al.*, Color catalogue of life in ice: Surface biosignatures on icy worlds. *Astrobiology* **22**, 313–321 (2022).
19. D. Nesvorný *et al.*, OSSOS XX: The meaning of Kuiper belt colors. *Astron. J.* **160**, 46 (2020).
20. C. Meinert *et al.*, Ribose and related sugars from ultraviolet irradiation of interstellar ice analogs. *Science* **352**, 208–212 (2016).
21. M. Nuevo, G. Cooper, S. A. Sandford, Deoxyribose and deoxysugar derivatives from photoprocessed astrophysical ice analogues and comparison to meteorites. *Nat. Commun.* **9**, 5276 (2018).
22. P. de Marcellus *et al.*, Aldehydes and sugars from evolved precometary ice analogs: Importance of ices in astrochemical and prebiotic evolution. *Proc. Natl. Acad. Sci. U.S.A.* **112**, 965–970 (2015).
23. M. Pasek, D. Lauretta, Extraterrestrial flux of potentially prebiotic C, N, and P to the early Earth. *Orig. Life. Evol. Biosph.* **38**, 5–21 (2008).
24. D. Nesvorný *et al.*, Origin and evolution of short-period comets. *Astrophys. J.* **845**, 27 (2017).
25. D. P. Cruikshank, H. Imanaka, C. M. Dalle Ore, Tholins as coloring agents on outer Solar System bodies. *Adv. Space Res.* **36**, 178–183 (2005).
26. C. Sagan, B. N. Khare, Tholins: Organic chemistry of interstellar grains and gas. *Nature* **277**, 102–107 (1979).
27. C. M. Dalle Ore *et al.*, Organic materials in planetary and protoplanetary systems: Nature or nurture?. *Astron. Astrophys.* **533**, A98 (2011).
28. S. C. Tegler, W. Romanishin, S. J. G. J. Consolmagno, Color patterns in the Kuiper belt: A possible primordial origin. *Astrophys. J.* **599**, L49 (2003).
29. W. R. Thompson, B. G. J. P. T. Murray, B. N. Khare, C. Sagan, Coloration and darkening of methane clathrate and other ices by charged particle irradiation: Applications to the outer solar system. *J. Geophys. Res.* **92**, 14933–14947 (1987).
30. E. Quirico *et al.*, On a radiolytic origin of red organics at the surface of the Arrokoth Trans-Neptunian Object. *Icarus* **394**, 115396 (2023).
31. J. Luu, D. Jewitt, Color diversity among the Centaurs and Kuiper belt objects. *Astron. J.* **112**, 2310–2318 (1996).
32. S. A. Stern, Evidence for a collisional mechanism affecting Kuiper belt object colors. *Astron. J.* **124**, 2297 (2002).
33. R. Gil-Hutton, Color diversity among Kuiper belt objects: The collisional resurfacing model revisited. *Planet. Space Sci.* **50**, 57–62 (2002).
34. S. D. Benecchi *et al.*, The correlated colors of transneptunian binaries. *Icarus* **200**, 292–303 (2009).
35. W. M. Grundy, Is the missing ultra-red material colorless ice? *Icarus* **199**, 560–563 (2009).
36. M. D. Melita, Z. Kaňuchová, R. Brunetto, G. Strazzulla, Space weathering and the color–color diagram of Plutinos and Jupiter Trojans. *Icarus* **248**, 222–229 (2015).
37. R. Brunetto, M. A. Barucci, E. Dotto, G. Strazzulla, Ion irradiation of frozen methanol, methane, and benzene: Linking to the colors of centaurs and trans-neptunian objects. *Astrophys. J.* **644**, 646–650 (2006).
38. M. J. Poston *et al.*, Visible near-infrared spectral evolution of irradiated mixed ices and application to Kuiper belt objects and jupiter trojans. *Astrophys. J.* **856**, 124 (2018).
39. J. M. Hollis, F. J. Lovas, P. R. Jewell, Interstellar glycolaldehyde: The first sugar. *Astrophys. J.* **540**, L107–L110 (2000).
40. C. J. Bennett, R. I. Kaiser, On the formation of glycolaldehyde ($HCOCH_2OH$) and methyl formate ($HCOOCH_3$) in interstellar ice analogs. *Astrophys. J.* **661**, 899–909 (2007).
41. T. Mathew, P. M. Esteves, G. K. S. Prakash, Methanol in the RNA world: An astrochemical perspective. *Front. Astron. Space Sci.* **9**, 809928 (2022).
42. K. I. Öberg, R. T. Garrod, E. F. van Dishoeck, H. Linnartz, Formation rates of complex organics in UV irradiated CH3OH-rich ices. I. Experiments. *Astron. Astrophys.* **504**, 891–913 (2009).
43. G. Strazzulla, J. F. Cooper, E. R. Christian, R. E. Johnson, Ion irradiation of TNOs: From the fluxes measured in space to the laboratory experiments. *C. R. Phys.* **4**, 791–801 (2003).
44. D. C. Jewitt, From Kuiper belt object to cometary nucleus: The missing ultrared matter. *Astron. J.* **123**, 1039–1049 (2002).
45. M. E. Brown, E. L. Schaller, W. C. Fraser, A hypothesis for the color diversity of the Kuiper belt. *Astrophys. J. Lett.* **739**, L60 (2011).
46. N. Peixinho, A. Delsanti, A. Guilbert-Lepoutre, R. Gafeira, P. Lacerda, The bimodal colors of Centaurs and small Kuiper belt objects. *Astron. Astrophys.* **546**, A86 (2012).
47. D. Jewitt, Color systematics of comets and related bodies. *Astron. J.* **150**, 201 (2015).

48. J. F. Cooper, E. R. Christian, J. D. Richardson, C. Wang, Proton irradiation of centaur, Kuiper belt, and oort cloud objects at plasma to cosmic ray energy. *Earth, Moon and Planets* **92**, 261–277 (2003).
49. M. J. Loeffler, P. D. Tribbett, J. F. Cooper, S. J. Sturner, A possible explanation for the presence of crystalline H_2O-ice on Kuiper belt objects. *Icarus* **351**, 113943 (2020).
50. S. Maity, R. I. Kaiser, B. M. Jones, Formation of complex organic molecules in methanol and methanol–carbon monoxide ices exposed to ionizing radiation–a combined FTIR and reflectron time-of-flight mass spectrometry study. *Phys. Chem. Chem. Phys.* **17**, 3081–3114 (2015).
51. A. M. Turner, R. I. Kaiser, Exploiting photoionization reflectron time-of-light mass spectrometry to explore molecular mass growth processes to complex organic molecules in interstellar and solar system ice analogs. *Acc. Chem. Res.* **53**, 2791–2805 (2020).
52. M. J. Abplanalp, M. Förstel, R. I. Kaiser, Exploiting single photon vacuum ultraviolet photoionization to unravel the synthesis of complex organic molecules in interstellar ices. *Chem. Phys. Lett.* **644**, 79–98 (2016).
53. S. P. D. Birch, O. M. Umurhan, Retention of CO ice and gas within 486958 Arrokoth. *Icarus* **413**, 116027 (2024).
54. C. J. Bennett, S.-H. Chen, B.-J. Sun, A. H. H. Chang, R. I. Kaiser, Mechanistical studies on the irradiation of methanol in extraterrestrial ices. *Astrophys. J.* **660**, 1588–1608 (2007).
55. C. S. Jamieson, A. M. Mebel, R. I. Kaiser, Understanding the kinetics and dynamics of radiation-induced reaction pathways in carbon monoxide ice at 10 K. *Astrophys. J. Suppl. Ser.* **163**, 184–206 (2006).
56. J. X. Luu, D. C. Jewitt, Charge-coupled device spectra of asteroids. I. Near-earth and 3: 1 resonance asteroids. *Astron. J.* **99**, 1985–2011 (1989).
57. S. Jester *et al.*, The sloan digital sky survey view of the palomar–green bright quasar survey. *Astron. J.* **130**, 873–895 (2005).
58. O. R. Hainaut, H. Boehnhardt, S. Protopapa, Colours of minor bodies in the outer solar system. *Astron. Astrophys.* **546**, A115 (2012).
59. R. B. Woodward, Structure and the absorption spectra of α, β-unsaturated ketones. *J. Am. Chem. Soc.* **63**, 1123–1126 (1941).
60. L. F. Fieser, M. Fieser, S. Rajagopalan, Absorption spectroscopy and the structures of the diosterols. *J. Org. Chem.* **13**, 800–806 (1948).
61. C. Zhu, A. M. Turner, C. Meinert, R. I. Kaiser, On the production of polyols and hydroxycarboxylic acids in interstellar analogous ices of methanol. *Astrophys. J.* **889**, 134 (2020).
62. E. Hénault *et al.*, Widespread CO_2 and CO in the trans-neptunian population revealed by JWST/DiSCo-TNOs. ResearchSquare [Preprint] (2023). https://doi.org/10.21203/rs.3.rs-2887978/v1 (Accessed 29 July 2023).
63. M. E. Brown, W. C. Fraser, The state of CO and CO_2 ices in the Kuiper belt as seen by JWST. *Planet. Sci. J.* **4**, 130 (2023).
64. C. Zhang *et al.*, Processing of methane and acetylene ices by galactic cosmic rays and implications to the color diversity of Kuiper Belt objects. *Sci. Adv.* **9**, eadg6936 (2023).
65. S. Pilling *et al.*, Understanding the molecular kinetics and chemical equilibrium phase of frozen CO during bombardment by cosmic rays by employing the PROCODA code. *Astrophys. J.* **952**, 17 (2023).
66. C. J. Bennett, C. P. Ennis, R. I. Kaiser, Experimental studies on the formation of D_2O and D_2O_2 by implantation of energetic D^+Ions into oxygen Ices. *Astrophys. J.* **782**, 62 (2014).
67. C. Meinert, U. J. Meierhenrich, A new dimension in separation science: Comprehensive two-dimensional gas chromatography. *Angew. Chem. Int. Ed.* **51**, 10460–10470 (2012).
68. T. Stephan, TOF-SIMS in cosmochemistry. *Planet. Space Sci.* **49**, 859–906 (2001).
69. L. Bernard, R. Crockett, M. Kawecki, Monosaccharides: A ToF-SIMS reference spectra database. I. Negative polarity. *Surf. Sci. Spectra* **26**, 025001 (2019).
70. L. Bernard, R. Crockett, M. Kawecki, Monosaccharides: A ToF-SIMS reference spectra database II. Positive polarity. *Surf. Sci. Spectra* **26**, 025002 (2019).
71. E. N. Tokareva, A. V. Pranovich, B. R. Holmbom, Characteristic fragment ions from lignin and polysaccharides in ToF–SIMS. *Wood Sci. Technol.* **45**, 767–785 (2010).
72. T. Stephan, E. Jessberger, C. Heiss, D. Rost, TOF–SIMS analysis of polycyclic aromatic hydrocarbons in Allan Hills 84001. *Meteorit. Planet. Sci.* **38**, 109–116 (2002).
73. J. Abplanalp Matthew, R. Frigge, I. Kaiser Ralf, Low-temperature synthesis of polycyclic aromatic hydrocarbons in Titan's surface ices and on airless bodies. *Sci. Adv.* **5**, eaaw5841 (2019).
74. J. Luu, D. Jewitt, Reflection spectrum of the Kuiper belt object 1993 SC. *Astron. J.* **111**, 499–503 (1996).
75. S. C. Tegler, W. Romanishin, S. J. G. J. Consolmagno, Two color populations of Kuiper belt and centaur objects and the smaller orbital inclinations of red centaur objects. *Astron. J.* **152**, 210 (2016).
76. A. Doressoundiram, H. Boehnhardt, S. C. Tegler, C. Trujillo, "Color properties and trends of the transneptunian objects" in *The Solar System Beyond Neptune*, M. A. Barucci, H. Boehnhardt, D. P. Cruikshank, A. Morbidelli (The University of Arizona Space Science Series, Arizona, AZ, 2008), pp. 91–104.
77. D. Bodewits *et al.*, The carbon monoxide-rich interstellar comet 2I/Borisov. *Nat. Astron.* **4**, 867–871 (2020).
78. M. Bouilloud *et al.*, Bibliographic review and new measurements of the infrared band strengths of pure molecules at 25 K: H_2O, CO_2, CO, CH_4, NH_3, CH_3OH, HCOOH and H_2CO. *Mon. Not. R. Astron. Soc.* **451**, 2145–2160 (2015).
79. A. M. Turner *et al.*, A photoionization mass spectroscopic study on the formation of phosphanes in low temperature phosphine ices. *Phys. Chem. Chem. Phys.* **17**, 27281–27291 (2015).
80. D. Drouin *et al.*, CASINO V2.42–A fast and easy-to-use modeling tool for scanning electron microscopy and microanalysis users. *Scanning* **29**, 92–101 (2007).
81. A. Yeghikyan, Evolution of energetic particle fluxes in the early heliosphere. *Astrophysics* **60**, 374–386 (2017).
82. C. J. Bennett, C. Pirim, T. M. Orlando, Space-weathering of solar system bodies: A laboratory perspective. *Chem. Rev.* **113**, 9086–9150 (2013).
83. R. E. Johnson, Irradiation effects in a comet's outer layers. *J. Geophys. Res. Planets* **96**, 17553–17557 (1991).
84. R. E. Johnson, *Energetic Charged-Particle Interactions with Atmospheres and Surfaces, Physics and Chemistry in Space* (Springer, Berlin, Heidelberg, 1990), 10.1007/978-3-642-48375-2, p. 84.
85. G. J. Golabek, M. Jutzi, Modification of icy planetesimals by early thermal evolution and collisions: Constraints for formation time and initial size of comets and small KBOs. *Icarus* **363**, 114437 (2021).
86. S. S. Prasad, S. P. Tarafdar, UV radiation field inside dense clouds – Its possible existence and chemical implications. *Astrophys. J.* **267**, 603–609 (1983).
87. C. J. Bennett, C. S. Jamieson, Y. Osamura, R. I. Kaiser, A combined experimental and computational investigation on the synthesis of acetaldehyde [$CH_3CHO(X^1A')$] in interstellar ices. *Astrophys. J.* **624**, 1097 (2005).
88. B. M. Jones, R. I. Kaiser, Application of reflectron time-of-flight mass spectroscopy in the analysis of astrophysically relevant ices exposed to ionization radiation: Methane (CH_4) and D_4-methane (CD_4) as a case study. *J. Phys. Chem. Lett.* **4**, 1965–1971 (2013).
89. M. J. Abplanalp, B. M. Jones, R. I. Kaiser, Untangling the methane chemistry in interstellar and solar system ices toward ionizing radiation: A combined infrared and reflectron time-of-flight analysis. *Phys. Chem. Chem. Phys.* **20**, 5435–5468 (2018).
90. G. M. Muñoz Caro *et al.*, Comparison of UV and high-energy ion irradiation of methanol:ammonia ice. *Astron. Astrophys.* **566**, A93 (2014).
91. G. A. Baratta, G. Leto, M. E. Palumbo, A comparison of ion irradiation and UV photolysis of CH_4 and CH_3OH. *Astron. Astrophys.* **384**, 343–349 (2002).
92. C. R. Arumainayagam *et al.*, Extraterrestrial prebiotic molecules: Photochemistry vs. radiation chemistry of interstellar ices. *Chem. Soc. Rev.* **48**, 2293–2314 (2019).
93. G. Tarczay, M. Forstel, P. Maksyutenko, R. I. Kaiser, Formation of higher silanes in low-temperature silane (SiH_4) ices. *Inorg. Chem.* **55**, 8776–8785 (2016).
94. P. B. Crandall, J. J. Gillis-Davis, R. I. Kaiser, Untangling the origin of molecular hydrogen in the lunar exosphere. *Astrophys. J.* **887**, 27 (2019).